INTERNATIONAL JOURNAL FOR NUMERICAL METHODS IN FLUIDS
Int. J. Numer. Meth. Fluids 2003; **43**:979–1001 (DOI: 10.1002/fld.518)

Computation of an unsteady complex geometry flow using novel non-linear turbulence models

Paul G. Tucker*,†, Yan Liu, Yongmann M. Chung and Alex Jouvray

Fluid Dynamics Research Centre, The University of Warwick, Coventry, CV4 7AL, U.K.

SUMMARY

Non-linear zonal turbulence models are applied to an unsteady complex geometry flow. These are generally found to marginally improve predicted turbulence intensities. However, relative to linear models, convergence is mostly difficult to achieve. Clipping of some non-linear Reynolds stress components is required along with velocity field smoothing or alternative measures. Smoothing is naturally achieved through multilevel convergence restriction operators. As a result of convergence difficulties, generally, non-linear model computational costs detract from accuracy gains. For standard Reynolds stress model results, again computational costs are prohibitive. Also, mean velocity profile data accuracies are found worse than for a simple mixing length model. Of the non-linear models considered, the explicit algebraic stress showed greatest promise with respect to accuracy and stability. However, even this shows around a 30% error in total (the sum of turbulence and unsteadiness) intensity. In strong contradiction to measurements the non-linear and Reynolds models predict quasi-steady flows. This is probably a key reason for the total intensity under-predictions. Use of LES in a non-linear model context might help remedy this modelling aspect. Copyright © 2003 John Wiley & Sons, Ltd.

KEY WORDS: turbulence; large eddy simulation; Reynolds stress models; non-linear; explicit algebraic stress model

1. INTRODUCTION

Franke and Rodi [1], Johansson, Davidson and Olsson [2], Przulj and Younis [3], Durbin [4] and Bosch and Rodi [5] make unsteady Reynolds averaged Navier–Stokes (URANS) predictions for vortex shedding behind cylinders. These studies clearly demonstrate the unsteady flow modelling deficiencies of linear eddy viscosity models. Notably, the dissipative standard k–ε model erroneously gives rise to steady flow. Tucker and Pan [6] makes URANS computations for flow in the complex congested Figure 1 geometry (an idealized electronics system). The flow is driven by two fans. A wide range of linear turbulence models are tried. These give significantly different turbulent kinetic energy (k) values and hence eddy viscosities (μ_t).

* Correspondence to: P. G. Tucker, School of Engineering, The University of Warwick, Coventry, CV4 7AL, U.K.
† E-mail: p.tucker@warwick.ac.uk

Contract/grant sponsor: Engineering and Physical Sciences Research Council (EPSRC); contract/grant number: GR/No.5581

Received 3 March 2002
Revised 19 January 2003

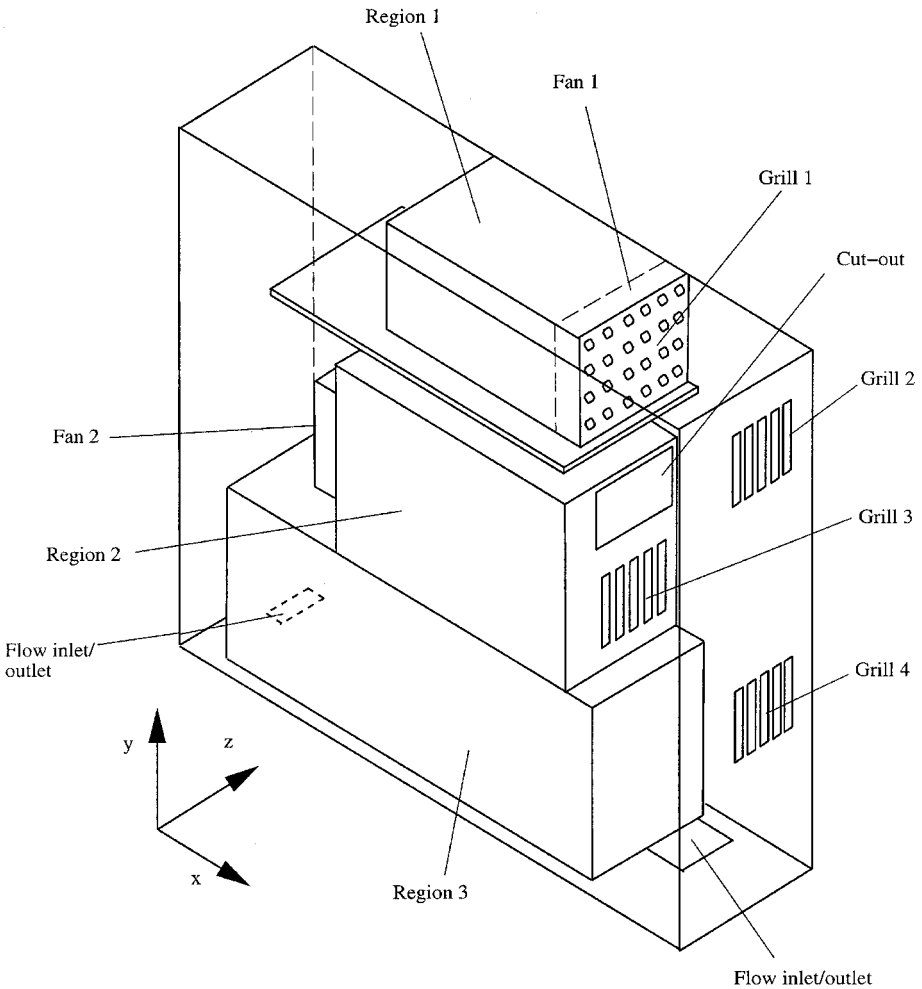

Figure 1. Schematic of idealized system considered.

The latter parameter, as would be expected, greatly impacts on predicted unsteadiness amplitudes. Based on the above linear URANS model poor performances, further outlined in Reference [7], attention is being turned to non-linear models. These potentially can account for turbulence anisotropy more economically than full Reynolds stress models (RSM). Tatsumi *et al.* [8] make non-linear URANS predictions for flow over a backwards facing step. Kimura and Hosoda [9], revisit the computation of flow around square cylinders using an essentially non-linear type model (see Reference [10]). Barakos and Drikakis [11] consider the non-linear model prediction of airfoil shock induced oscillations. The above non-linear results are quite inconclusive. Although, large eddy simulation (LES) and Reynolds stress models sometimes show greater potential than linear model URANS predictions (see References [12, 13]) they are computationally expensive. Also, the latter (see References [14, 15]) are not without empirical content and controversies regarding wall reflection terms and adequacy when

modelling streamline curvature effects. Therefore, potentially computationally less expensive, non-linear models are here further explored using the demanding Figure 1 geometry/flow. The dissipation rate (ε) transport equation is generally considered to be a problematic element of turbulence closures. Potential, complex geometry, tending to transitional Reynolds number flow modelling improvements, due to the ε modifications of Yap [16] and Nishimura *et al.* [12] are considered. The former is an ε transport equation source term extension and the latter a boundary condition variant. To more readily put non-linear eddy viscosity model performances into context, one RSM prediction is presented and comparison made with LES data. Zero equation models such as the mixing length are popular in electronics cooling design. This is partly because electronics systems frequently comprise numerous channel like regions. Therefore, as a baseline, zero and also (on potential computational efficiency grounds) one equation model results are presented. Although, predictions for other non-linear turbulence stress relationships are considered [10, 17], results mostly focus on the classical relationship of Speziale [18] in a zonal context. This is because of its k–l based LES [19, 20] and zonal LES extension [21] potential.

2. NUMERICAL METHOD

Following Johansson *et al.* [2], and Bosch and Rodi [5] and based on experimental and numerical evidence for the current flow, the governing equations are presented in a phase averaged [‡] tensor form. Conservation of momentum can be expressed as

$$\frac{\partial\langle U_i\rangle}{\partial t}+\frac{\partial\langle U_i\rangle\langle U_j\rangle}{\partial x_j}=-\frac{1}{\rho}\frac{\partial\langle P\rangle}{\partial x_i}+\frac{\mu}{\rho}\frac{\partial}{\partial x_j}\left(\frac{\partial\langle U_i\rangle}{\partial x_j}+\frac{\partial\langle U_j\rangle}{\partial x_i}\right)+\frac{\partial\langle-\overline{u_i'u_j'}\rangle}{\partial x_j} \tag{1}$$

where $\langle U\rangle$ is an averaged fluid velocity component, u' is the averaged turbulence fluctuating component, ρ the fluid density, μ viscosity, $\langle P\rangle$ averaged static pressure, t time and x the spatial co-ordinate. The corresponding continuity equation is as follows:

$$\frac{\partial\langle U_j\rangle}{\partial x_j}=0 \tag{2}$$

2.1. 'Boussinesq' approximations

The role of the turbulence model is to approximate Equation (1), $\langle-\rho\overline{u_i'u_j'}\rangle$, Reynolds stress terms. To do this the following 'Boussinesq' approximations are considered:

$$\langle-\overline{u_i'u_j'}\rangle=\left[-n_0\frac{2}{3}\langle k\rangle\delta_{ij}+2\frac{\mu_t^*}{\rho}S_{ij}\right]_{\mathrm{L}}+n_1\left[\tilde{A}\frac{\mu_t^*}{\rho}\frac{\langle k\rangle}{\langle\varepsilon\rangle}\left(S_{ik}S_{kj}-\frac{1}{3}S_{kl}S_{kl}\delta_{ij}\right)+\tilde{E}\right]_{\mathrm{NL}} \tag{3}$$

where S_{ij} is the mean strain rate. In the above, $n_1=0$ gives a standard linear Boussinesq approximation for which $\mu_t^*=\mu_t$. For $n_1=1$ the non-linear models are gained. The forms of $\tilde{A}$, $\tilde{E}$ and μ_t^* for the non-linear model of Speziale [18], the cubic and also the explicit algebraic

[‡] Alternatively, it is also possible to view Equation (1) as being time averaged over a short period say T which is much smaller than the time scale of the mean flow variations, thus ensuring time scale separation.

stress can be found in Appendix A. In Equation (3) subscripts L and NL are used to represent linear and non-linear contributions. Generally $n_0 = 1$ but for the mixing length model $n_0 = 0$.

2.2. Turbulence energy, dissipation and stress transport equations

When $\langle k \rangle$ is required, the following differential transport equation is used

$$\frac{\partial \langle \Phi \rangle}{\partial t} + \frac{\partial \langle U_j \rangle \langle \Phi \rangle}{\partial x_j} = \frac{1}{\rho} \frac{\partial}{\partial x_j} \left(\Gamma_\phi \frac{\partial \langle \Phi \rangle}{\partial x_j} \right) + T_1 + T_2 + T_3 \tag{4}$$

where $\langle \Phi \rangle = \langle k \rangle$, $\Gamma_k = \mu + \mu_t/\sigma_k$ (σ_k is the diffusion Prandtl number for k), $T_1 = -\langle \overline{u_i' u_j'} \rangle \partial \langle U_i \rangle / \partial x_j$ (turbulence production), $T_2 = -\langle \varepsilon \rangle$ (the rate of dissipation of turbulence kinetic energy) and $T_3 = 0$. By setting $\langle \Phi \rangle = \langle \varepsilon \rangle$, $\Gamma_\varepsilon = \mu + \mu_t/\sigma_\varepsilon$ (where σ_ε is the diffusion Prandtl number for ε), $T_1 = -\langle \overline{u_i' u_j'} \rangle \partial \langle U_i \rangle / \partial x_j C_{\varepsilon 1} \langle \varepsilon \rangle / \langle k \rangle$, $T_2 = -C_{\varepsilon 2} \langle \varepsilon \rangle^2 / \langle k \rangle$ and

$$T_3 = C_w \frac{\langle \varepsilon \rangle^2}{\langle k \rangle} \max \left[\left(\frac{\langle k \rangle^{3/2}}{\langle \varepsilon \rangle l} - 1 \right) \left(\frac{\langle k \rangle^{3/2}}{\langle \varepsilon \rangle l} \right)^2, 0 \right] \tag{5}$$

(where $l = C_l y$) an $\langle \varepsilon \rangle$ equation is gained. The final T_3 term is an optional extension of the standard equation derived by Yap [16]. It is usually *most* active just outside the viscous sub-layer, a region which in a high-Reynolds number computation is covered with wall-functions. For some, less general, modelling approaches, the rate of dissipation is related to normal wall distances. The technique for evaluating these is described later. When $\langle \Phi \rangle = \langle \overline{u_i' u_j'} \rangle$, Equation (4) can also serve as a Reynolds stress transport equation. For stability, in this, following Lien and Leschziner [22] turbulent and molecular diffusion can both be accounted for through $\Gamma_{\overline{u_i' u_j'}} = \mu + \mu_t/\sigma_{\overline{u_i' u_j'}}$. Advantageously, the Reynolds stress transport equation has an exact turbulence production representation $T_1 = -(\overline{\langle u_i' u_k' \rangle} \partial \langle U_j \rangle / \partial x_k + \overline{\langle u_j' u_k' \rangle} \partial \langle U_i \rangle / \partial x_k)$. To dissipate turbulence $T_2 = 2\delta_{ij} \langle \varepsilon \rangle / 3$. T_3 can now be considered to represent the problematic pressure strain term (normally symbolically represented as ϕ_{ij}). Avoiding the need to model wall reflection terms, as used in the linear Gibson and Launder [23] type modelling, the quadratic pressure strain model of Speziale *et al.* [24] is selected.

The various models used will now be outlined. The differences between linear and non-linear models is in essence minor, being reflected through the terms included in the Boussinesq approximation embodied in Equation (3). Unless otherwise stated $n_0 = n_1 = 1$ in Equation (3) giving non-linear models. The different models will now be described. Each is given a different label. The subscripts l and h are used to identify low and high Reynolds number models, respectively. Subscripts 1, 2 and 3 are also used to identify use of the models of [18] (nl_1), [10] (nl_2) and [17] (nl_3), respectively. The great majority of predictions presented here use the non-linear model of Speziale [18] (nl_1).

2.3. Mixing length model

For reference purposes a standard mixing length (ml_1) model is used. For this

$$\mu_t = \rho \langle l_\mu \rangle^2 \left[2 \frac{\partial \langle U_i \rangle}{\partial x_j} S_{ij} \right]^{1/2} \tag{6}$$

where $\langle l_\mu \rangle = \kappa y(1-\mathrm{e}^{-\langle y^+ \rangle/26})$ is a Van Driest damped mixing length. In this $\langle y^+ \rangle = y\sqrt{\rho\langle \tau_w \rangle}/\mu$, $\langle \tau_w \rangle$ is the averaged wall shear stress and κ the Von Karman constant. Outside the near wall region $\langle l_\mu \rangle = \kappa\langle \delta \rangle$ where $\langle \delta \rangle$ is an approximation to the boundary layer thickness. A differential equation based approach is used to evaluate wall distance [6]. This approach gives nearest and furthest wall distances and the average of these is used to estimate $\langle \delta \rangle$.

2.4. *nl–k–l models*

The non-linear k–l (nl–k–l) models are implemented through Wolfshtein's [25] linear k–l model. Equation (4) is solved for $\langle \Phi \rangle = \langle k \rangle$, and $\langle \varepsilon \rangle$ defined using

$$\langle \varepsilon \rangle = \frac{\langle k \rangle^{3/2}}{\langle l_\varepsilon \rangle} \tag{7}$$

where $\langle l_\varepsilon \rangle = C_{\varepsilon 0} y(1 - n_2 \mathrm{e}^{-A_\varepsilon \langle y^+ \rangle / C_\mu^{1/4}})$ and $\langle y^+ \rangle = y\rho\langle k \rangle^{1/2} C_\mu^{1/4}/\mu$. The turbulent viscosity can be expressed as

$$\mu_t = \rho C_\mu \langle l_\mu \rangle \langle k \rangle^{1/2} \tag{8}$$

where $\langle l_\mu \rangle = C_{\mu 0} y(1 - n_2 \mathrm{e}^{-A_\mu \langle y^+ \rangle / C_\mu^{1/4}})$. When $n_2 = 1$, the length scales $\langle l_\varepsilon \rangle$ and $\langle l_\mu \rangle$ have Wolfshtein's damping functions giving a low Reynolds number non-linear model designated here the nl–k–l_1. Predictions are also made with $n_2 = 0$ and computationally economical logarithmic wall functions (see Reference [26]). This, high Reynolds number, model is called here the nl–k–l_h model.

2.5. *nl–k–ε model*

For the non-linear k–ε model, Equation (4) is solved with $\langle \Phi \rangle = \langle k \rangle$ and $\langle \varepsilon \rangle$ and the turbulent viscosity found using

$$\mu_t = \rho C_\mu \frac{\langle k \rangle^2}{\langle \varepsilon \rangle} \tag{9}$$

For results presented, near walls one of the following is applied:

(I) the standard logarithmic wall functions [26] (nl–k–ε_h);
(II) the de-sensitized ε boundary condition of Nishimura *et al.* [12];
(III) the near wall modelling modifying source term of Yap [16] and
(IV) simplified low Reynolds number turbulence models.

2.6. *Zonal models*

With these, for $\langle y^+ \rangle \geqslant 60$ the nl–k–ε method is used and for $\langle y^+ \rangle < 60$ the k–l_1 or nl–k–l_1 models are applied. To connect the differing models at the $\langle y^+ \rangle = 60$ interface the following patching condition is required:

$$\langle \varepsilon \rangle = \langle k \rangle^{3/2}/\langle l_\mu \rangle \tag{10}$$

Two non-linear approaches are tried. These are designated the nl–k–ε_h/k–l_1 and nl–k–ε_h/nl–k–l_1. The latter is fully non-linear. The former uses a linear near wall model (i.e. for $\langle y^+ \rangle < 60$, $n_1 = 0$).

As noted earlier, for all the models discussed above, their linear counterparts can be fully recovered by setting $n_1 = 0$ in Equation (3). These linear variants will be compared with later and are identified by omission of the *nl* prefix.

2.7. Features specific to non-linear models

Non-linear equation (3) contributions are differentiated and directly incorporated into (1) and (4). For the nl_1 model following [18], for stability, velocities in the non-linear part of the 'Boussinesq' approximation are smoothed. Here, an 18-point distance weighted averaging is used. The averaging is performed using multigrid restriction operators (see Reference [7]).

Speziale's model approximation often yields stresses that do not satisfy realizability needs. For channel flows (see Reference [27]) near walls, streamwise normal stresses $\overline{u_1' u_1'}$ become excessively high ($40u_\tau^2$). Also, $\overline{u_2' u_2'}$ and $\overline{u_3' u_3'}$ can become negative (ensuring the sum of the three components is equal to k) with greater magnitudes than correct positive values. However, Speziale's original model (nl_1) readily transfers into a low Reynolds number form [28] where, fortunately, the aforementioned poor behaviour (in the greater part due to the Oldroyd derivatives) mostly goes. Tests, not presented here, show the lack of high Reynolds number model realizability (i.e. the negative and excessively high normal stresses) can partly give rise to numerical instabilities. These are found especially severe for relatively low Reynolds number flows such as found in electronics (a strong focus of this paper). For these flows, near wall y^+ values tend to be low and as suggested by Mompean *et al.* [27], in this situation the realizability problem noted above becomes worse with negative normal stress component magnitudes increasing. Therefore, especially for the complex Figure 1 geometry clipping on non-linear 'Boussinesq' contributions appears warranted. In the current discretization process contributions to the turbulence equations are split into two parts. The non-linear ($\partial\langle -\overline{u_i' u_j'}\rangle_{\mathrm{NL}}/\partial x_j$) contributions are treated as source terms. Linear contributions ($\partial\langle -\overline{u_i' u_j'}\rangle_{\mathrm{L}}/\partial x_j$) are distributed between the diffusion and source terms, the $2\langle k\rangle\delta_{ij}/3$ term going to the source. For all predictions, an initially linear solution is produced and then the non-linear source term is included in the computation. Two clipping approaches are tried. Either the magnitude of the non-linear contribution to the total Reynolds stress component is limited to be less than some multiple of the value arising from the linear part of (3), i.e.

$$|\langle -\overline{u_i' u_j'}\rangle|_{\mathrm{NL}} = \min[\beta\langle -\overline{u_i' u_j'}\rangle_{\mathrm{L}}, |\langle -\overline{u_i' u_j'}\rangle|_{\mathrm{NL}}] \tag{11}$$

Alternatively, gradient contributions (effectively non-linear source term contributions) are limited, for each individual tensor component, in a similar way as follows:

$$\left|\frac{\partial\langle -\overline{u_i' u_j'}\rangle_{\mathrm{NL}}}{\partial x_j}\right| = \min\left[\beta\left|\frac{\partial\langle -\overline{u_i' u_j'}\rangle_{\mathrm{L}}}{\partial x_j}\right|, \left|\frac{\partial\langle -\overline{u_i' u_j'}\rangle_{\mathrm{NL}}}{\partial x_j}\right|\right] \tag{12}$$

The latter approach avoids large non-linear contribution gradient discontinuities. Therefore, this approach is perhaps to be preferred. Incidentally, the use of clipping to enforce turbulence model realizability is not new (see, for example, References [29, 30]). For the nl_1–k–l_h, nl_1–k–l_l, nl_1–k–ε/k–l, nl_1–k–ε/nl_1–k–l and nl_2–k–ε_h models clipping is based on 200, 20, 200, 100 and 100%, respectively, of linear model values. These values correspond to $\beta = 2, 0.2, 2, 1$ and 1 and are more motivated/based on stability rather than turbulence physics grounds. Of all the non-linear models, the nl_2 perhaps seemed the most stable and with care it is expected

that clipping may not be required. For the cubic model clipping was not required. However, to gain converged solutions non-linear terms had to be introduced very gradually in a staged fashion. Also, on turbulence physics grounds C_μ was clipped with a maximum value of 0.09.

The following standard model constants are used: $\sigma_k = 1$ (0.82 for RSM), $\sigma_\varepsilon = 1.3$, $\sigma_{\overline{u_i' u_j'}} = 0.82$, $A_\varepsilon = 0.263$, $A_\mu = 0.016$, $C_{\varepsilon 0} = 2.4$, $C_{\varepsilon 1} = 1.44$, $C_{\varepsilon 2} = 1.92$, $C_{\mu 0} = 2.4$, $C_\mu = 0.09$, $C_w = 0.83$, $C_l = 2.55$, $\kappa = 0.41$, $E \approx 9.0$. Other constant values specific to the different non-linear models can be found in Appendix A.

2.8. Turbulence intensities

The flow to be studied is unsteady. Consequently, the measured instantaneous velocity u is the sum of U (the time-averaged velocity component, i.e. not the total velocity) and fluctuations due to turbulence u' and also unsteadiness u'' (i.e. $u = U + u' + u''$ or $u = \langle U \rangle + u'$). Measurements of turbulence intensity to be compared with have not been corrected for the effect of flow unsteadiness. These intensities can be expressed as

$$T_i' = \frac{\sqrt{\overline{(u' + u'')^2}}}{U} \tag{13}$$

Experimental data comparisons are made with predictions of T_i (where the periodic fluctuation is filtered out, i.e. only the modelled turbulence u' is considered in Equation (13)) and T_i'.

2.9. General program features

Generally, the flow governing equations are solved using the NEAT finite volume program (see Reference [7]). Normal wall distances required in some turbulence models are calculated using a novel differential equation based technique [32]. Mostly, a fully implicit time scheme is used. Diffusion terms are treated in a second-order fashion. Generally, the second-order central difference based CONDIF [31] convective term treatment is implemented. This involves parameters such as $R_{x\phi} = (\partial\phi/\partial x)^+/(\partial\phi/\partial x)^-$ where the '+' and '−' superscripts identify gradients to the right and left of a central grid point. Variables $R_{y\phi}$ and $R_{z\phi}$ are defined in a similar way to $R_{x\phi}$. If the ϕ distribution is locally constant $R_{i\phi} = 0$. In steep gradient regions it can become high. Therefore, for numerical reasons, a limit is set on $R_{i\phi}$ such that $1/R_{\max} \leqslant R \leqslant R_{\max}$. In Reference [31] it is proposed typically $R_{\max}$ is between 4 and 10. Examination of the CONDIF equations shows reducing $R_{\max}$ corresponds to introducing false diffusion. Indeed for $R_{\max} = 1$ CONDIF becomes equivalent to first-order upwinding. A key CONDIF aspect is that for $R_{i\phi} < 0$ (i.e. at flow maxima and minima) first-order upwinding is explicitly enforced. Generally, according to Runchal [31], for most flows, $R_{i\phi} < 0$ at just a small number of grid points.

For the 'one-off' Reynolds stress model predictions, to save coding effort a commercial program is used [33]. In this, the CONDIF option is not available and instead second-order upwinding is implemented. Also, for nl_2 and nl_3 results, to aid convergence the hybrid (first-order upwind for Peclet numbers over two) scheme is used.

2.10. Boundary conditions

Appropriate Dirichlet or differential boundary conditions are set depending on the flow direction. For example, at outflow boundaries, the gradients of variables are set to zero in

a second-order fashion and the total pressure fixed. The slotted grills 1–4 (see Figure 1) are modelled using established loss coefficients. Fans are treated using quadratic momentum sources. Further boundary condition information can be found in Reference [6]. Of especial relevance here, for the high Reynolds number k–ε model, based on dimensional analysis the following first off-wall boundary condition is appropriate

$$\langle \varepsilon \rangle = C \frac{\langle k \rangle^{3/2}}{y} \tag{14}$$

where in the standard model (see Reference [26])

$$C = \frac{C_\mu^{3/4}}{\kappa} \tag{15}$$

The above C is only really applicable for $y^+ > 30$. However, as noted earlier, for low Reynolds number complex geometry flows in can be difficult to ensure first off-wall grid nodes are positioned in accordance with the above y^+ limitation. Therefore, Nishimura *et al.* [12] propose the following direct numerical simulation (DNS) data fit based C expression.

$$C = \max[0.19, 7.90(y^+)^{-1.89}] \tag{16}$$

Performance of the above two (Equations (15) and (16)) boundary condition expressions is compared later. For the RSM, Equation (4) is solved for k and ε throughout the complete flow domain with ε evaluated at boundary nodes using (14). Therefore, considering equilibrium and a log based near wall profile at first off-wall grid nodes

$$\langle \overline{u_{i,j}'^2} \rangle = C \langle k \rangle \tag{17}$$

where $C = 1.098, 0.247, 0.655, -0.255$ depending on the set stress component.

2.11. Numerical details

Predictions are made using a base grid with about 0.4 million generally regular hexahedral control volumes. These are constructed so that at first off-wall grid nodes y^+_{ave} is around 2 and 15 for the low and high Reynolds number turbulence model predictions, respectively. To check for grid independence a NEAT prediction is made on a DEC super scalar computer with around 4 million control volumes (for details of this expensive simulation see Reference [34]). It is attempted to keep the grid structures on the commercial and NEAT codes as similar as possible. For stable and time step independent predictions, typically time steps of $\Delta t = 0.001\,\text{s}$ are used. However, for non-linear model stability, on average time-steps are generally 30% lower than this value. The average cell Courant number is always less than 1×10^{-2} and often much lower than this. Generally, on average, non-linear model under-relaxation factor values are just under half those used for linear models.

Where complex geometry predictions and measurements are spatially compared, percentage errors are given. The following experimental data point summations are made

$$\text{Error}_U = \frac{\sum_{\text{exp}} |\phi_{\text{exp}} - \phi_{\text{num}}|}{U_0}, \quad \text{Error}_{T_i} = \frac{\sum_{\text{exp}} |\phi_{\text{exp}} - \phi_{\text{num}}|}{\sum_{\text{exp}} |\phi_{\text{exp}}|} \tag{18}$$

where, U_0 is the approximate average return flow velocity for the system, obtained by integrating over velocity profiles ($U_0 \approx 1.5\,\text{m/s}$) and ϕ_{exp} corresponds to an experimental data

point and ϕ_{num} a numerical value. Where numerical data points do not coincide exactly with measurements a stiff quadratic spline interpolation is used.

3. RESULTS AND DISCUSSION

3.1. Temporal accuracy validation

To explore NEAT's temporal accuracy the propagation of a subcritical ($Re = 500$) Tollmien–Schlichting (TS) wave in plane Poiseuille flow is explored. Plate 1(a) shows x–y plane CONDIF disturbance stream function contours with $R_{\max} = 5$. As can be seen, the expected cellular 'structure' appearance is correctly captured. Plates 2(b)–2(e) give CONDIF contours of R_{xu}, R_{yu}, R_{xv} and R_{yv}, respectively. The significant white coloured zones correspond to negative $R_{i\phi}$ first-order upwind regions. The colour extremes show where false diffusion is introduced through the $R_{\max} = 5$ limit. Figure 2 compares predicted and analytical x direction variations of vertical velocity fluctuations (v') at the channel centre line. Symbols represent the Orr-Sommerfeld analytical solution. CONDIF second-order central differencing and upwinding along with first-order upwinding and hybrid are represented by the lines. The results confirm the codes temporal accuracy, with the second-order central differencing and upwind (which is used for the RSM prediction) schemes agreeing with the analytical solution. The graph well illustrates the strong damping effect of first-order upwinding and hence hybrid. Consequently, the CONDIF's first-order upwind component is seen to have a clear accuracy influence. However, its predictive accuracy is still significantly better than that for the hybrid scheme. Also, it is considered that the present case is perhaps not especially good for illustrating CONDIF performance. This is because, for such a simple geometry, $R_{i\phi}$ is negative or its magnitude high at quite a large percentage of grid points. This point is enforced by Plate 2, instantaneous k–l_h model, mid x–y plane plots. Frame (a) gives a velocity vector plot. Frames (b)–(e) give CONDIF contours of R_{xu}, R_{yu}, R_{xv} and R_{yv}, respectively. As can be seen the areas where first-order upwinding is used are relatively low.

It seems worth noting here that channel flow predictions, similar to those considered for the TS wave, involving SIMPLE, SIMPLEC, AVPI [7], PISO and a fractional step method

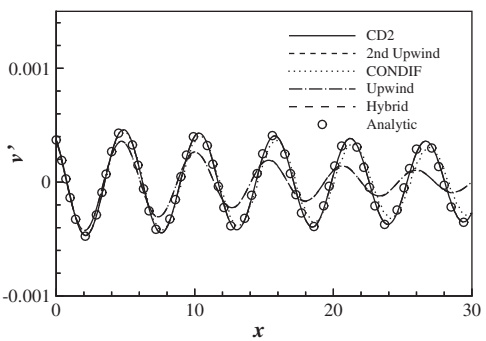

Figure 2. Comparison of various discretization schemes.

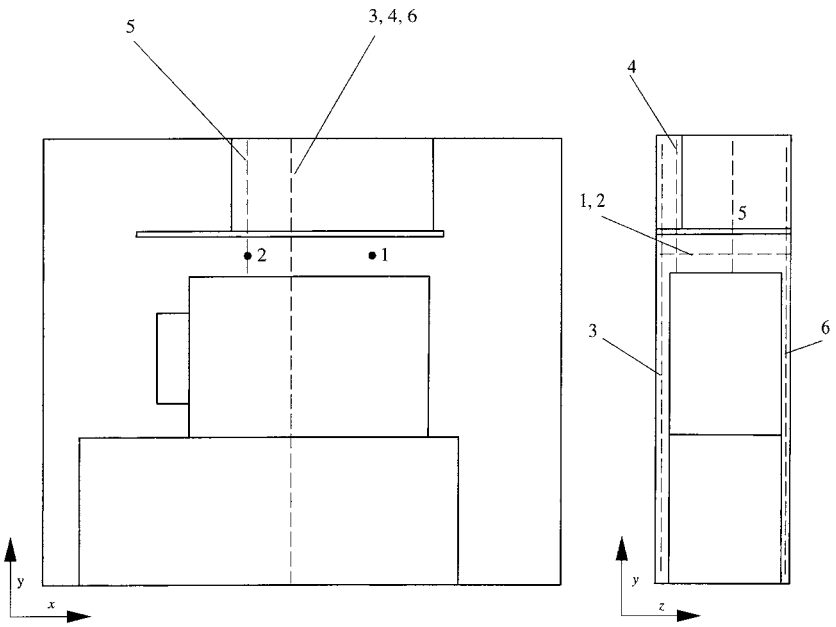

Figure 3. Positions of velocity and turbulence intensity profiles.

(for a higher channel flow Reynolds number) show insignificant performance differences and so the choice of SIMPLE seems justified.

3.2. Non-linear term validation cases

To validate the newly added non-linear 'Boussinesq' terms, computations for some relatively simple steady flows are considered. Some of these are presented in Appendix B. The cases considered involve fully developed two- and three-dimensional channel flows and the separated flow over a backward facing step. For the two-dimensional channel flow, comparison is made with the Reynolds stress component measurements of Laufer [35]. All, the non-linear models are found to give improved agreement. For the three-dimensional channel it is verified that Prandtl motions of the second kind are predicted, thus giving further confidence that the extensive non-linear terms are correctly coded. For the step case, the prediction of reattachment lengths is considered. For non-linear models, improved agreement is found with the data of Kim [36]. The above give confidence in the implementation of the non-linear terms and now the complex Figure 1 flow system is considered.

3.3. Complex geometry results

Comparisons are made with LDA measurements having an estimated accuracy $\pm 5\%$ along the lines/profiles shown in Figure 3. The exact locations of profiles 1–6 are: $X=0.53$, $Y=0.73$; $X=0.37$, $Y=0.73$; $X=0.41$, $Z=0.06$; $X=0.41$, $Z=0.10$; $X=0.37$, $Z=0.57$ and $X=0.41$, $Z=0.96$, respectively (X, Y and Z are dimensionless co-ordinates such that $X=Y=Z=1$ correspond

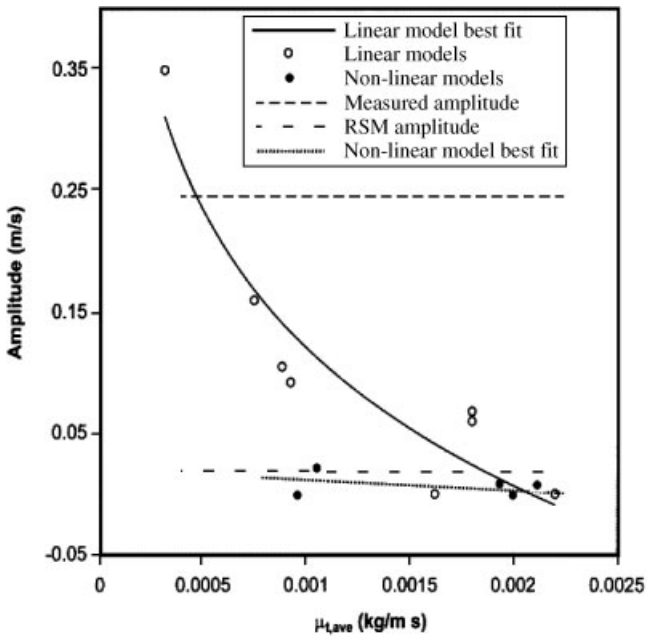

Figure 4. Variation of unsteadiness amplitude with turbulent viscosity.

to the maximum extent of the system). Comparisons are also made with thermistor based mean flow temporal velocity variation measurements with a $\pm 10\%$ accuracy for six points on profiles 1–6 (see Reference [6]). For this complex geometry flow, the older Van Driest damping functions are not used. Instead, generally Wolfshtein's are implemented. This is because the Figure 1 geometry flow has significant areas of separation (see later). Hence, use of the Van Driest function would seem a retrograde step.

3.4. Temporal velocity variations

The thermistor-based measurements show the average velocity unsteadiness amplitude is about 0.25 m/s. Figure 4, is a plot of averaged, predicted amplitude against turbulent viscosity for the different turbulence models. The amplitudes are based on velocity time traces at the centre of profiles 1–6 shown in Figure 3. The turbulent viscosity is calculated from a volume average over the complete domain. Open symbols represent linear turbulence model predictions, closed nl_1 non-linear and the full and dotted lines respective best fits to these. Each symbol represents a different turbulence model. The horizontal fine dashed line gives the measured average amplitude and the coarse dashed the RSM result. As can be seen, linear model amplitudes vary significantly, decreasing with increasing μ_t. This has some consistency with the observation of Brackenridge [37]. For the non-linear models, some linear momentum equation, Reynolds stress components are not incorporated through diffusion terms. Consequently, the trend of decreasing amplitude with increasing turbulent viscosity is no longer observed. Also, as with the RSM, unsteadiness amplitudes are too small.

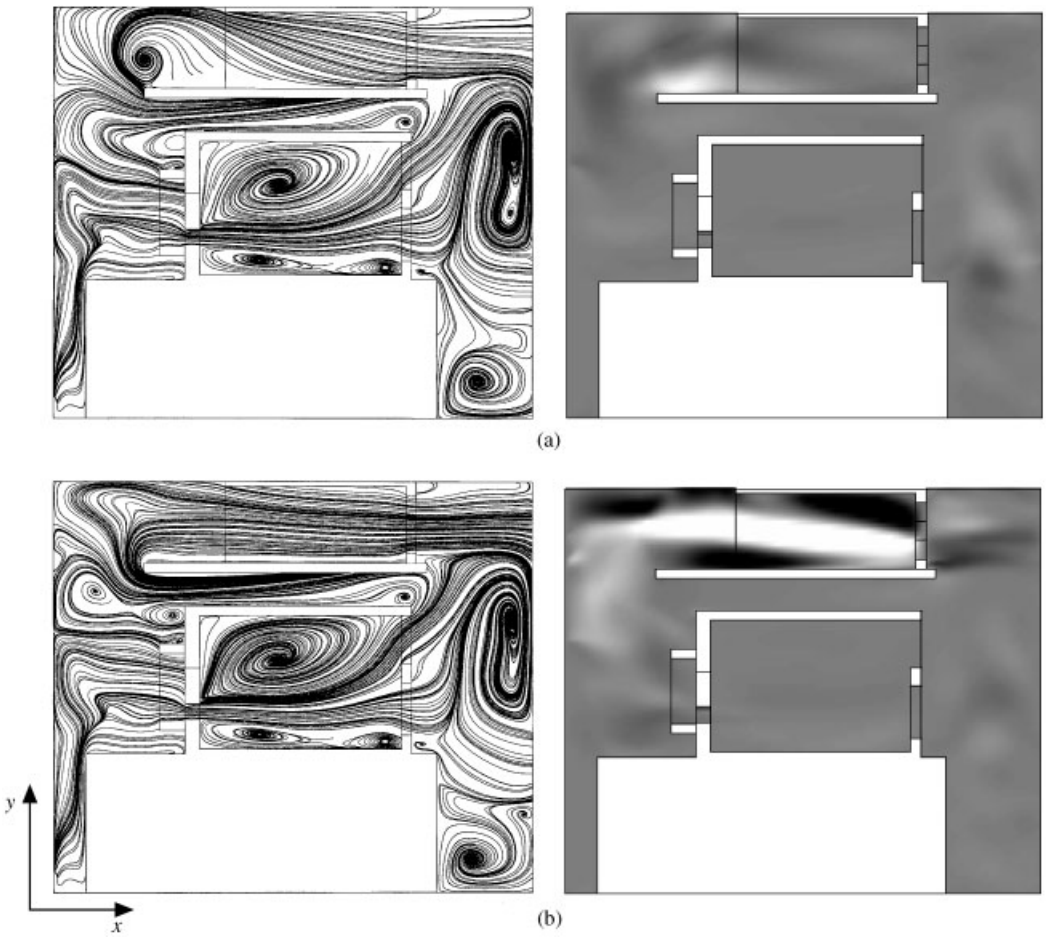

Figure 5. Plots of mid x–y plane streamlines and horizontal velocity component unsteadiness at: (a) $t^* \cong 0.125$ and (b) $t^* \cong 0.25$.

3.5. *Flow structure*

Figure 5, shows mid-axis x–y plane, k–l_1 model, instantaneous streamline and axial velocity ($\partial U/\partial t$) contour plots at approximately $t^* \cong 0.125$ and 0.25 corresponding to frames (a) and (b), respectively (note the dimensionless time is expressed as a fraction of one complete unsteadiness cycle). Plots suggest the major predicted unsteadiness source is separation arising from Fan 1 rapidly turning the flow through 180°. This, at $t^* \cong 0.125$ (Frame (a)) causes massive x–y plane separation. At $t^* \cong 0.25$ (Frame (b)) the vortex arising from separation collapses. The collapse and regeneration of this vortex repeats exactly in time. For non-linear nl_1 solutions the flow is either fixed in a separated or attached mode, the attached being the preferred. More detailed plots exploring the above limit cycle behaviour can be found in Reference [6].

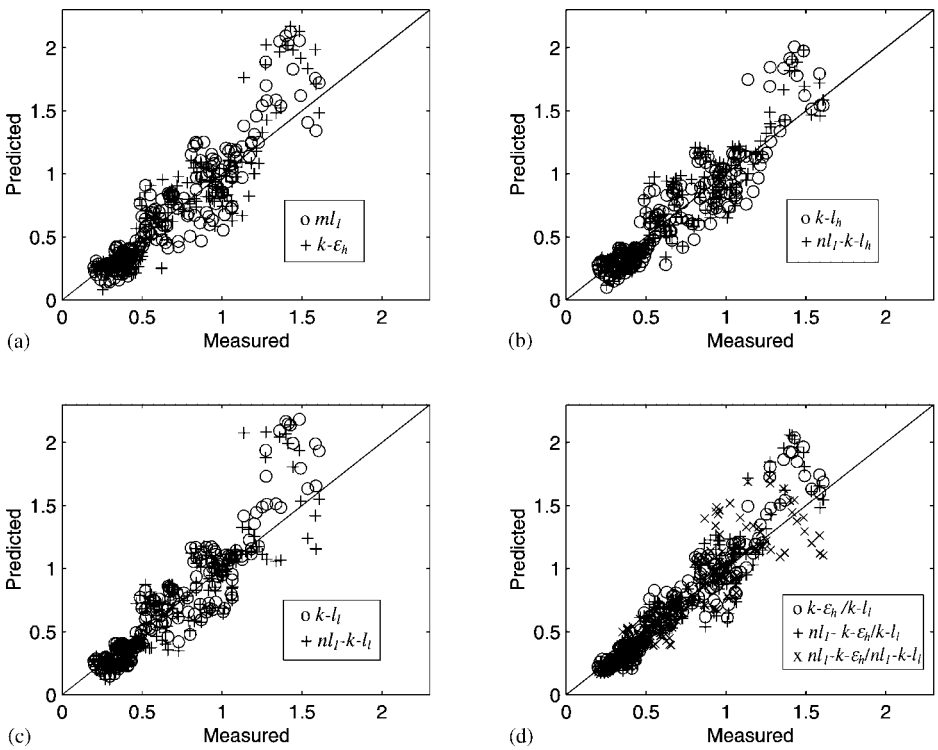

Figure 6. Plots of measured against predicted velocities for profiles 1–6.

3.6. *Velocity and intensity magnitude comparisons*

Figure 6, plots measured against predicted velocities for profiles 1–6. If agreement is perfect the symbols should fall on the 45° reference line. Frame (a) gives ml_1 and k–ε_h results, (b) k–l_h and nl_1–k–l_h, (c) k–l_1 and nl_1–k–l_1 and (d) k–ε/k–l_1, nl_1–k–ε/k–l_1 and nl_1–k–ε/nl_1–k–l_1 results. Mixing length predictions are included for interest representing the simplest useful engineering turbulence model. A key point is that most measured points tend to be positioned under the line, i.e. velocities returned by the different models are low. The percentage error (velocity and intensity) for each Figure 6 profile and model is summarized in Table I. Smagorinsky model based LES data of Chung *et al.* [38] is also included along with the RSM data. The average velocity profile error for the different models is around 18%, mostly corresponding to an under prediction of magnitudes. The various models deviate from this average by about ±3.0%. The table shows the RSM and k–ε_h models have a similar velocity accuracy to the mixing length. The poor k–ε_h model performance is not remedied by the Yap term or Nishimura *et al.* modification. Therefore, these results and those for its non-linear counterpart will not be further considered. The key Table I observation is that for the present complex flow, inclusion of non-linear terms or RSM use has overall not helped velocity predictions. Also, the LES predictions have better velocity accuracy than the RSM.

Table I. Summary of percentage errors.

Model	Error$_U$	Error$_{Ti'}$
ml_l	21	—
k–l_h	18	−53 (−56)
nl_l–k–l_h	17	−52 (−52)
k–l_l	19	−47 (−50)
nl_l–k–l_l	19	−45 (−46)
k–ε_h	20	—
k–ε/k–l_l	15	−34 (−34)
nl_l–k–ε/k–l_l	17	−33 (−33)
nl_l–k–ε/nl_l–k–l_l	16	−33 (−33)
nl_2–k–ε_h	17	−30 (−30)
nl_3–k–ε_h	15	−39 (−39)
RSM	20	−25 (−25)
LES	17	—

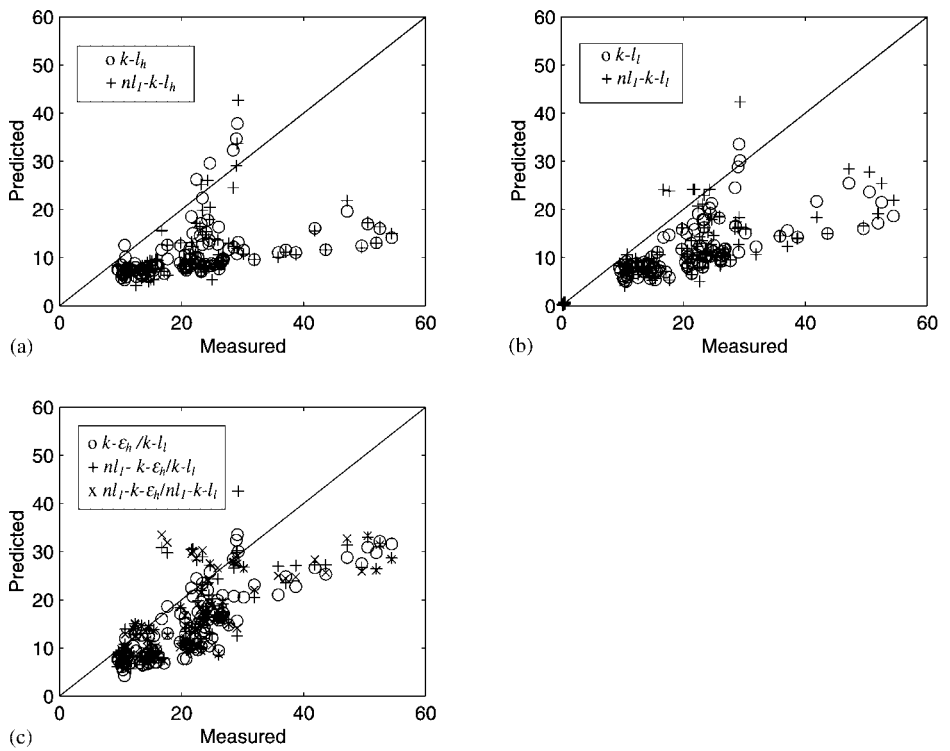

Figure 7. Plots of measured against predicted intensities for profiles 1–6.

Figure 7, shows the equivalent plot to Figure 6 (ignoring the ml and k–ε_h models) for T_i'. The key point to note is that intensities, like velocities, are generally under-predicted (the k–ε_h model in fact will badly over-predict intensities).

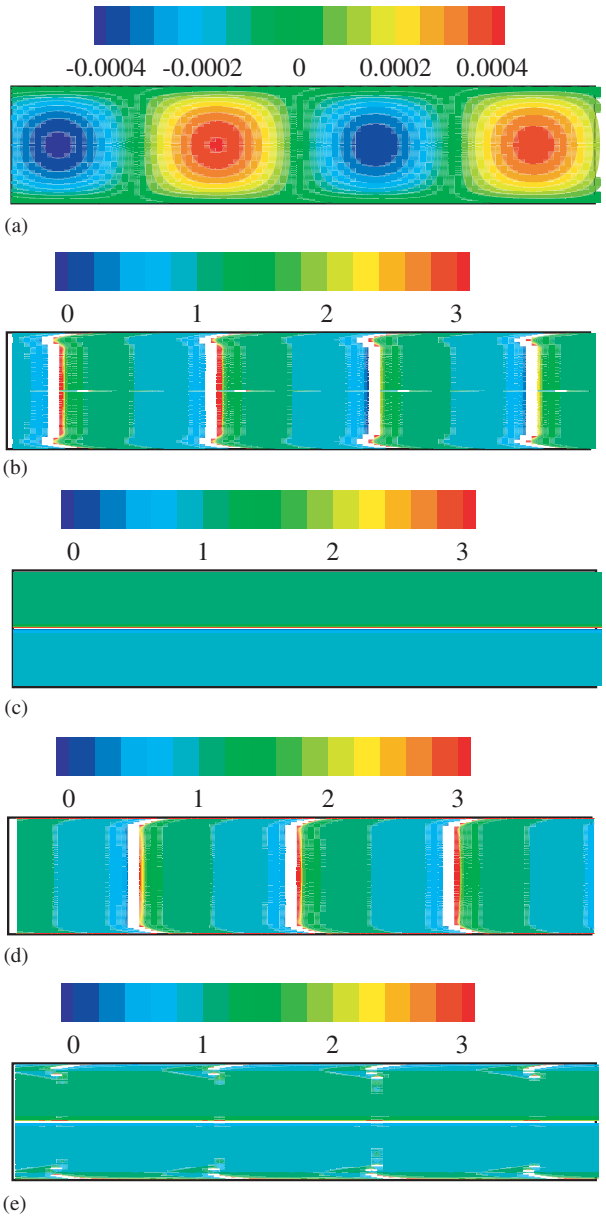

Plate 1.

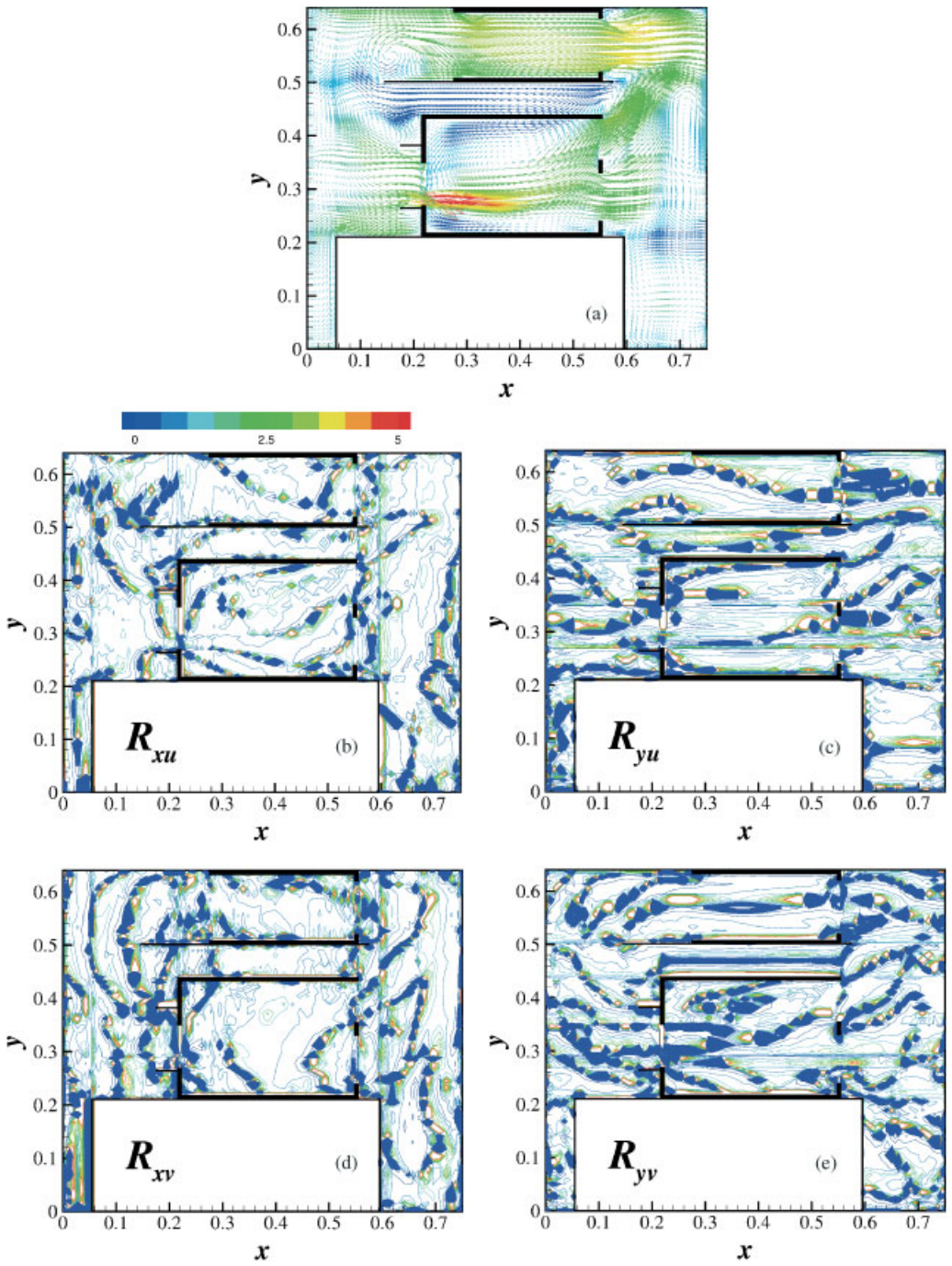

Plate 2.

Percentage total intensity, T_i', errors for all models are summarized on the right-hand side column of Table I. The minus signs reflect an under-prediction. The terms in parenthesis represent average T_i (i.e. true turbulence intensities containing just the stochastic turbulent component) error values. Generally, non-linear models appear to give T_i improvements. This is to be expected. Observation of the simple Appendix B channel flow results (in essence much of Figure 1 geometry consists of a series of channels) show inclusion of the non-linear terms increases the streamwise normal Reynolds stress. However, considering its satisfactory performance in validation tests, the nl_3 model performance for the Figure 1 geometry is surprisingly poor. This might be because it is used in a high Reynolds number form.

Figure 8, gives raw velocity profile data for the six Figure 3 profiles. The symbols represent measurements and the lines nl_2–k–ε_{h} results. Figure 9 is a repeat of Figure 8 but this time for turbulence intensity data. The key point to note is that changing to the explicit algebraic stress model has not produced any dramatic performance gains. Although improved, turbulence intensity errors are still significant.

The k–l_{h} linear and nl_1 based models have virtually identical convergence rates. However, the nl_1–k–l_1 model is at least 10 times more expensive than its linear counterpart. For the nl_1 zonal models, with linear wall modelling there is a cost increase factor of at least 2.5. Totally non-linear nl_1 zonal modelling appears to be over 5 times more expensive. Bearing all this in mind, any accuracy improvements seem rather small. Of note, Apsley and Leschziner [39] apply the nl_1 approximation (in a k–ε framework) to some relatively simple flow geometries. To gain convergence, drastically, it was found necessary to omit the Oldroyd derivative ($\overset{\circ}{S}_{ij} = 0$). Here convergence is secured by smoothing, clipping and use of relatively small under-relaxation parameters and time-steps. The latter gives Courant numbers of less than 0.001 and strong diagonal dominance. However, even with the listed stability measures, average non-linear model convergence errors below 0.75% are difficult to achieve. As shown in Reference [7], such levels will give satisfactory unsteadiness amplitudes and mean profile predictions but significant unsteadiness frequency errors (not of direct interest in the present work). Rokni and Sunden [40] improve Speziale's non-linear approximation convergence by utilizing the damping functions of Abe *et al.* [41]. Therefore, use of these functions might seem worth future exploration. The current results do suggest introduction of the Wolfshtein damping function detracts significantly from convergence.

Replacement of the nl_1 relationship with the explicit algebraic stress non-linear approximation of Abid *et al.* [10] shows evidence of improved convergence and smoothing is no-longer needed. However, nl_2 predictions for other geometries have shown serious stability problems. For the cubic model of Craft *et al.* [17] (nl_3) Reynolds stress clipping and smoothing are not needed. Even so convergence is difficult to secure. Quite elaborate measures involving the staged introduction of non-linear terms is required.

A more fruitful avenue of exploration for complex relatively low Reynolds number electronics geometries might be the use of zonal LES (see Reference [42]), where near walls, RANS models are applied and away from them LES implemented. Following Kosovic [20] the nl_1 relationship could be used as the basis for a k–l subgrid scale model. Such approaches possibly have greater longer-term accuracy benefits. However, for flows of especially low Reynolds number pure LES might be feasible. It is important to note that the Crank–Nicholson and second-order central difference based LES simulations of Chung *et al.* [38] show, unlike with the non-linear models, excellent convergence properties.

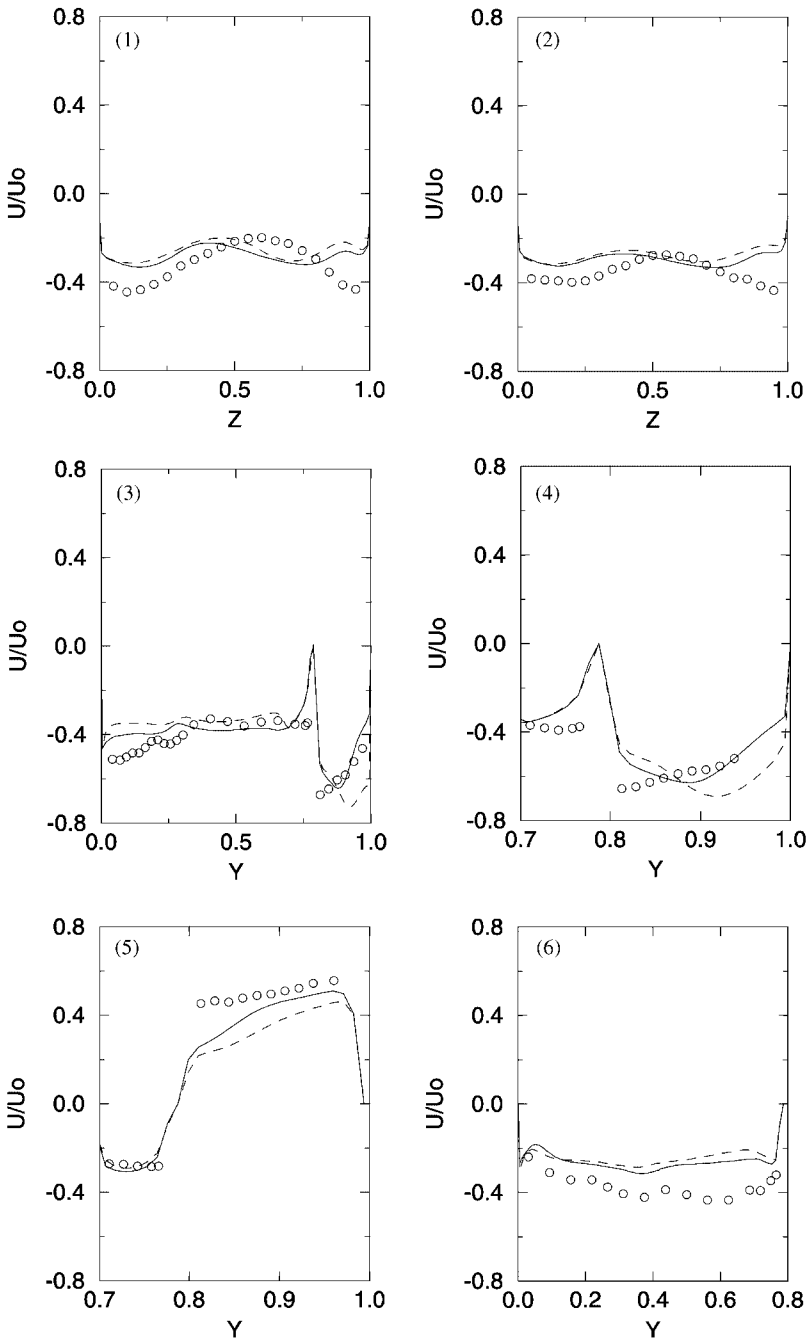

Figure 8. Comparison of velocity predictions with measurements for the k–ε_h and nl_2–k–ε_h (○, LDA measurements; ----, k–ε_h; —-, nl_2–k–ε_h).

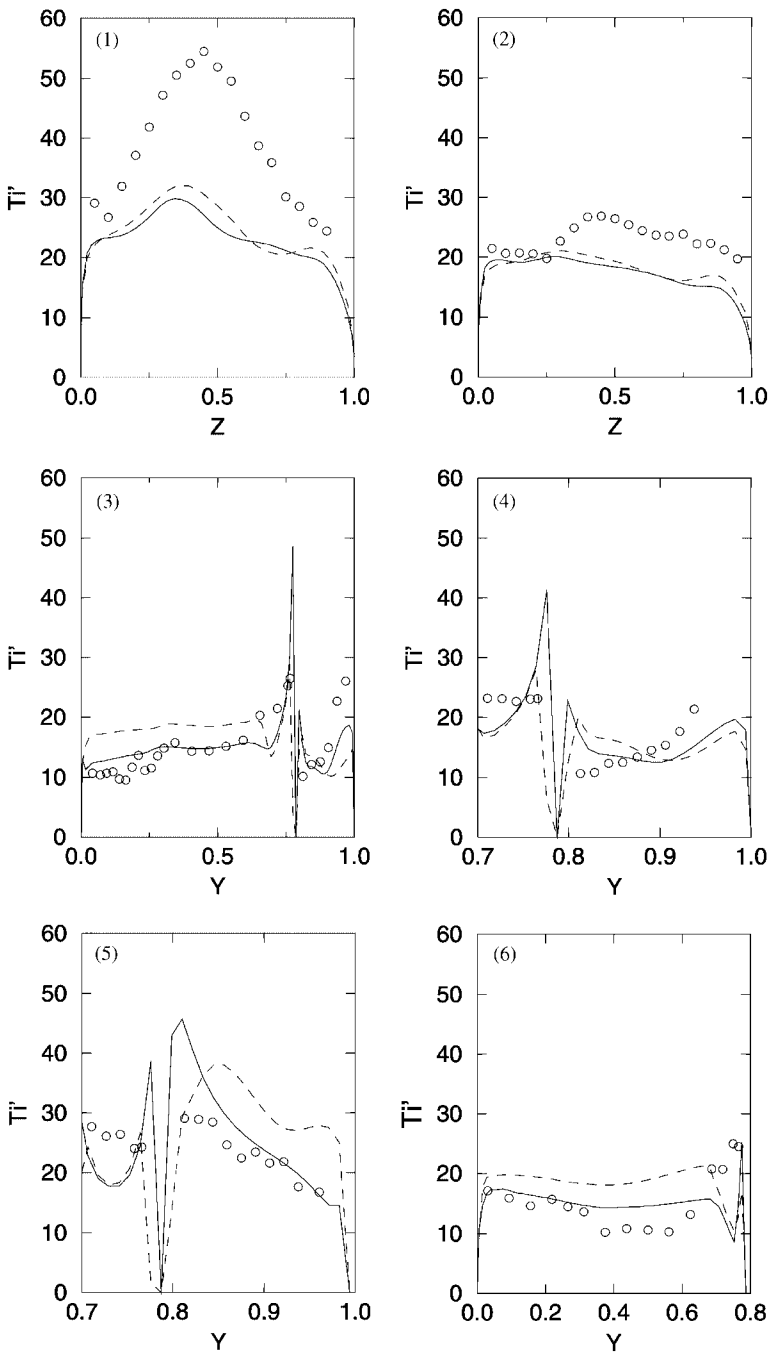

Figure 9. Comparison of intensity predictions with measurements for the k–ε_h and nl_2–k–ε_h (○, LDA measurements; ----, k–ε_h; —-, nl_2–k–ε_h).

4. CONCLUSIONS

For relatively simple geometries and steady flows non-linear models have seen significant testing showing some success. However, they have seen less use in highly complex geometries and unsteady flows such as the present. For such systems the additional terms introduced in the non-linear eddy viscosity relationship used here does not, generally, relative to computational cost, appear that beneficial. Also, for the present cases, the extra terms, relative to linear models, tend to damp unsteadiness. Although further testing is required, results suggest the simpler, more constrained models, at present, are perhaps (considering computational costs/non-linear model convergence difficulties) a sensible choice for many complex geometry applications. For higher accuracies, zonal models with more stable non-linear eddy viscosity and damping function relationships might be a sensible area of study. However, a more fruitful avenue of exploration for complex, relatively low Reynolds number electronics geometries might, be the use of non-linear zonal LES. Work in this area is currently being carried out using a classical non-linear relationship similar to Speziale's as a subgrid scale model. Also, the cubic model based zonal LES approach of Batten *et al.* [43] is being applied to complex geometry flows. Of the non-linear models the explicit algebraic stress showed greatest potential.

APPENDIX A

The forms of $\tilde{A}$, $\tilde{E}$ and μ_t^* used in Equation (3) are given below.

(1) *Speziale non-linear model*:

$$\tilde{E} = 4C_E C_\mu \frac{\mu_t^*}{\rho} \frac{\langle k \rangle}{\langle \varepsilon \rangle} \left(\overset{\circ}{S}_{ij} - \frac{1}{3} \overset{\circ}{S}_{kk} \delta_{ij} \right) \tag{A1}$$

In Equation (A1), $\overset{\circ}{S}_{ij}$, is the Oldroyd derivative is given by

$$\overset{\circ}{S}_{ij} = \frac{\partial S_{ij}}{\partial t} + \langle U_k \rangle \frac{\partial S_{ij}}{\partial x_k} - \frac{\partial \langle U_i \rangle}{\partial x_k} S_{kj} - \frac{\partial \langle U_j \rangle}{\partial x_k} S_{ki} \tag{A2}$$

$$\tilde{A} = 4C_D C_\mu \tag{A3}$$

$$\mu_t^* = \mu_t \tag{A4}$$

where $C_\mu = 0.09$, $C_D = C_E = 1.68$.

(2) *Craft et al. cubic model*:

$$\begin{aligned} \tilde{E} = {} & 4c_2 \frac{\mu_t^*}{\rho} \frac{\langle k \rangle}{\langle \varepsilon \rangle} (W_{ik} S_{kj} + W_{jk} S_{ki}) + 4c_3 \frac{\mu_t^*}{\rho} \frac{\langle k \rangle}{\langle \varepsilon \rangle} \left(W_{ik} W_{jk} - \frac{1}{3} W_{lk} W_{lk} \delta_{ij} \right) \\ & + 8c_4 \frac{\mu_t^*}{\rho} \frac{\langle k \rangle^2}{\langle \varepsilon \rangle^2} (S_{ki} W_{lj} + S_{kj} W_{li}) S_{kl} + 8c_5 \frac{\mu_t^*}{\rho} \frac{\langle k \rangle^2}{\langle \varepsilon \rangle^2} S_{ij} S_{kl} S_{kl} \\ & + 8c_6 \frac{\mu_t^*}{\rho} \frac{\langle k \rangle^2}{\langle \varepsilon \rangle^2} S_{ij} W_{kl} W_{kl} \end{aligned} \tag{A5}$$

$$\begin{aligned} \tilde{A} &= 4c_1 \\ \mu_t^* &= \mu_t \end{aligned} \tag{A6}$$

where $S_{ij} = \frac{1}{2}(\partial U_i/\partial x_j + \partial U_j/\partial x_i)$ is the mean strain rate tensor and $W_{ij} = \frac{1}{2}(\partial U_i/\partial x_j - \partial U_j/\partial x_i)$ is the mean vorticity tensor. The coefficients $c_1, c_2, c_3, c_4, c_5, c_6$ are $0.1, -0.1, -0.26, 10c_\mu^2, 5c_\mu^2$ and $-5c_\mu^2$, respectively, where

$$c_\mu = \frac{0.3}{1 + 0.35\{\max(\tilde{S}, \tilde{W})\}^{1.5}}[1 - \exp(-0.36\exp(0.75\max(\tilde{S}, \tilde{W})))] \tag{A7}$$

with $\tilde{S} = \langle k\rangle/\langle\varepsilon\rangle\sqrt{2S_{ij}S_{ij}}$ and $\tilde{W} = \langle k\rangle/\langle\varepsilon\rangle\sqrt{2W_{ij}W_{ij}}$.

(3) *Explicit algebraic stress model*:

$$\tilde{E} = 2\mu_t^*\left[-\frac{1}{3}S_{kk}\delta_{ij} + \alpha_3\frac{\langle k\rangle}{\langle\varepsilon\rangle}(S_{ik}W_{kj} + S_{jk}W_{ki})\right] \tag{A8}$$

$$\tilde{A} = -2\alpha_4 \tag{A9}$$

$$\mu_t^* = \rho\frac{3(1+\eta^2)\alpha_1}{3 + \eta^2 + 6\xi^2\eta^2 + 6\xi^2}\frac{\langle k\rangle^2}{\langle\varepsilon\rangle} \tag{A10}$$

where

$$\eta = \alpha_2(S_{ij}S_{ij})^{1/2}\frac{\langle k\rangle}{\langle\varepsilon\rangle}, \quad \xi = \alpha_3(W_{ij}W_{ij})^{1/2}\frac{\langle k\rangle}{\langle\varepsilon\rangle}$$

The constants $\alpha_1, \alpha_2, \alpha_3, \alpha_4$ are $0.1137, 0.0876, 0.1869, 0.1752$, respectively [10].

APPENDIX B

In this appendix non-linear model validation cases are presented. First, fully developed channel flow with $Re \simeq 32\,000$ (the characteristic length scale in Re is based on the channel half-width $h/2 = 0.03175\text{m}$) is considered. For this case just results for the low Reynolds number k–l_1 and nl_1–k–l_1 turbulence models are shown with the Van Driest damping function. Results for the explicit algebraic stress (nl_2) and cubic (nl_3) models show a similar level of performance. To ensure that at first off-wall grid nodes $y^+ < 1,65$ non-uniform, cross channel, y, grid spacings are required. Figures B1(a)–B1(c) compare predictions and measurements for the variation of normalized $\overline{u'u'}$, $\overline{v'v'}$ and $\overline{w'w'}$ against y/h, respectively. Measurements, by Laufer [35], are represented using symbols. The k–l_1 and nl_1–k–l_1 predictions are given by the dashed and full lines, respectively. As can be seen, the non-linear model gives improved agreement with the measurements.

It is well known that when the channel geometry is no longer assumed two dimensional the effects of anisotropy on flow structure can also be striking, with the generation of Prandtl motions of the second kind. Non-linear eddy viscosity models are capable of modelling these motions. Predictions of these, periodic in the x co-ordinate, for $Re = 2400$, with a 33×33 (y,z) grid, refined at solid surfaces, using the nl_1–k–l_1 model, are shown in Figure B2. Again the standard Van Driest damping function is used. Considering the DNS data Mompean *et al.* [27]

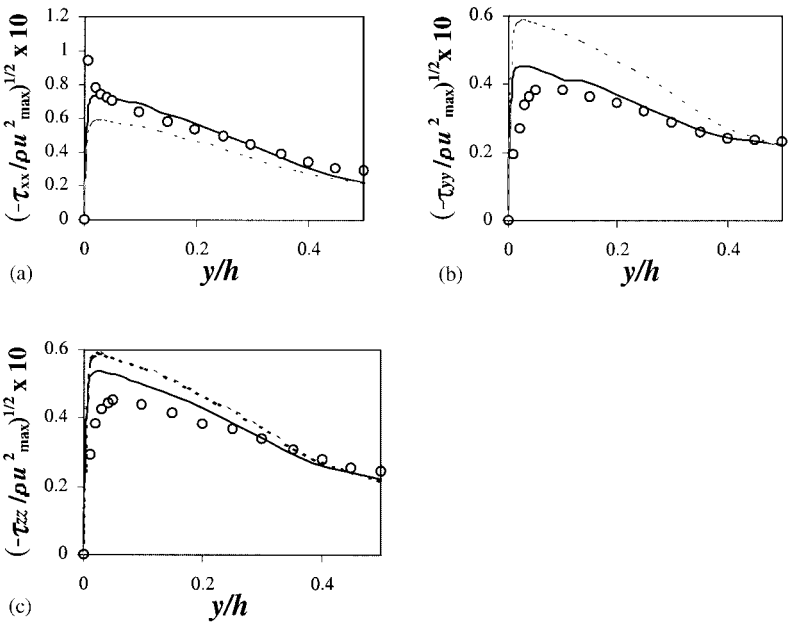

Figure B1. Comparisons of predictions and measurements for the variation of the normalized correlations $\overline{u'u'}$, $\overline{v'v'}$ and $\overline{w'w'}$ against y/h, respectively (○, experiment data; —, non-linear model; - - - - -, linear model).

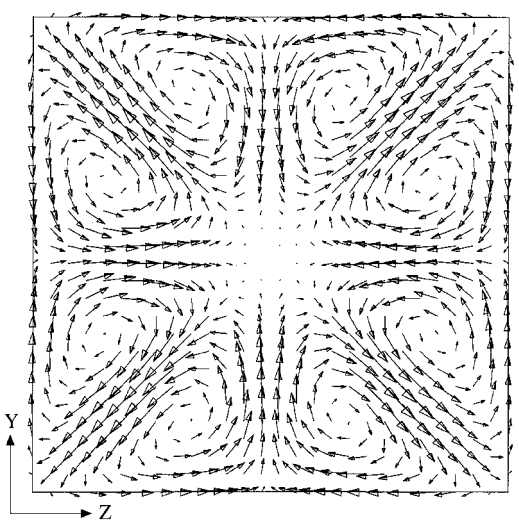

Figure B2. Predicted flow structure for a three-dimensional channel flow.

Table B1. Predicted reattachment lengths for backwards facing step flow.

Model	L/h_o
k–l_h	6.1
k–ε_h	6.0
nl_1–k–l_h	6.4
nl_1–k–ε_h	6.4
nl_2–k–ε_h	7.5
nl_3–k–ε_l	6.7
Exp.	7.0

shows that to gain the correct corner damping behaviour, the product of the two damping functions associated with the orthogonal walls can be taken. Therefore, the mixing length takes the following form:

$$\langle l_\mu \rangle = \kappa y(1 - e^{-\langle z^+ \rangle/26})(1 - e^{-\langle y^+ \rangle/26}) \tag{B1}$$

Without this approach, the y–z plane recirculations cannot be reproduced (It should be noted that Mompean *et al.*, do not use the standard Van Driest constants in their wall damping expression). However, there seems little use in adopting such a tuned approach and the use of standard constants is preferred here. The results give further confidence that the extensive non-linear terms have been correctly coded. The nl_2 and nl_3 models are also found to correctly predict the secondary motions.

The flow over a backward facing step is now considered. The predictive accuracy for the reattachment length, L, can be significantly improved with non-linear models. Table B1 shows predicted dimensionless reattachment lengths (L/h_o, where h_o is the step height) for the k–l_h, k–ε_h, nl_1–k–l_h, nl_1–k–ε_h, nl_2–k–ε_h and nl_3–k–ε_l models. These are for $Re = 132\,000$. The experimental L/h_o value is 7 (see Reference [36]). The improvement in predictive accuracy for anisotropy resolving techniques, which is due to better modelling of the Reynolds stresses, is clear.

ACKNOWLEDGEMENTS

Support from the Engineering and Physical Sciences Research Council (EPSRC) under grant number GR/NO5581 is gratefully acknowledged.

REFERENCES

1. Franke R, Rodi W. Calculation of vortex shedding past a square cylinder with various turbulence models. *Proceedings of the 8th International Symposium of Turbulent Shear Flows*, Munich, 1993; 189–204.
2. Johansson SH, Davidson L, Olsson E. Numerical simulation of vortex shedding past triangular cylinders at high Reynolds number using a k–ε turbulence model. *International Journal for Numerical Methods in Fluids* 1993; **16**:859–878.
3. Przulj V, Younis BA. Some aspects of the prediction of turbulent vortex shedding. *ASME Fluids Engineering Conference*, Washington, DC, FED-vol. 149, Separated Flows, 1993; 75–81.
4. Durbin PA. Separated flow computations with the k–ε–v^2 model. *AIAA Journal* 1995; **33**(4):659–664.
5. Bosch G, Rodi W. Simulation of vortex shedding past a square cylinder with different turbulence models. *International Journal for Numerical Methods in Fluids* 1998; **28**:601–616.
6. Tucker PG, Pan Z. URANS Computations for a complex internal isothermal flow. *Computer Methods in Applied Mechanics and Engineering* 2000; **190**:2893–2907.

7. Tucker PG. *Computation of Unsteady Internal Flows*. Kluwer Academic Publishers: Dordrecht, 2001.
8. Tatsumi K, Iwai H, Neo EC, Inaoka K, Suzuki K. Prediction of time-mean characteristics and periodical fluctuation of velocity and thermal fields of a backward-facing step. *Proceedings of the Ist International Symposium on Turbulence and Shear Flow*, Banerjee S, Eaton JK (eds), Santa Barbara, 1999; 139–144.
9. Kimure I, Hosoda T. 3-D unsteady flow structures around rectangular column in open channels by means of non-linear k–ε model. *Proceedings of the 1st International Symposium on Turbulence and Shear Flow*, Banerjee S, Eaton JK (eds), Santa Barbara, 1999; 1001–1006.
10. Abid R, Morrison HJ, Gatski TB. Prediction of aerodynamic flows with a new explicit algebraic stress model. *AIAA Journal* 1996; **34**(12):2632–2635.
11. Barakos G, Drikakis D. Numerical simulation of transonic buffet flows using various turbulence closures. *Proceedings of the 1st International Symposium on Turbulence and Shear Flow*, Banerjee S, Eaton JK (eds), Santa Barbara, 1999; 995–1000.
12. Nishimura M, Tokuhiro A, Kimura N, Kamide H. Numerical study on mixing of oscillating quasi-planar jets with low Reynolds number turbulent stress and heat flux equation models. *Nuclear Engineering and Design* 2000; **202**:77–95.
13. Pascal H, Jakirlic S, Hanjalic K. DNS and RANS-Modelling of in-cylinder turbulence subjected to axial compression. *Proceedings of the 3rd International Symposium on Turbulence Heat and Mass Transfer*, Nagoya, Japan, Nagano Y, Hanjalic K, Tsuji T (eds), vol. 3. Publisher: Aichi Shuppan, 2000; 479–486.
14. Spalart PR. Strategies for turbulence modelling and simulations. *International Journal of Heat and Fluid Flow* 2000; **21**:252–263.
15. Craft TJ, Launder BE. Application of TCL strategy to engineering and environmental flows. *Proceedings of the 2nd International Symposium on Advances in Computational Heat Transfer* (*CHT'01*), de Vahl Davis G, Leonardi E (eds), Australia, vol. 1, 2001; 15–30.
16. Yap CR. Turbulent heat and momentum transfer in recirculating impinging flows. *Ph.D. Thesis*, Department of Mechanical Engineering, Faculty of Technology, University of Manchester, 1987.
17. Craft TJ, Launder BE, Suga K. Development and application of a cubic eddy-viscosity model of turbulence. *International Journal of Heat and Fluid Flow* 1996; **17**:108–115.
18. Speziale CG. On non-linear k–l and k–ε models of turbulence. *Journal of Fluid Mechanics* 1987; **178**:459–475.
19. Wong VC. A proposed statistical-dynamic closure method for the linear or nonlinear subgrid-scale stresses. *Physics of Fluids* 1992; **4**:1080–1082.
20. Kosovic B. Subgrid scale modelling for the large eddy simulation of high Reynolds number boundary layers. *Journal of Fluid Mechanics* 1997; **336**:151–182.
21. Tucker PG, Davidson L. Zonal k–l based large eddy simulations. *Proceedings of the 41st Aerospace Sciences Meeting and Exhibit*, *AIAA*-2003-0082, 2003.
22. Lien FS, Leschziner MA. Assessment of turbulent transport models including non-linear RNG eddy-viscosity formulation and second-moment closure. *Computers and Fluids* 1994; **23**(8):983–1004.
23. Gibson MM, Launder BE. Ground effects on pressure fluctuations in the atmospheric boundary layer. *Journal of Fluid Mechanics* 1978; **86**:491–511.
24. Speziale CG, Sarkar S, Gatski TB. Modelling the pressure–strain correlation of turbulence: an invariant dynamical systems approach. *Journal of Fluid Mechanics* 1991; **227**:245–272.
25. Wolfshtein M. The velocity and temperature distribution in one-dimensional flow with turbulence augmentation and pressure gradient. *International Journal of Heat and Mass Transfer* 1969; **12**:301–318.
26. Launder BE, Spalding DB. The numerical computation of turbulent flows. *Computer Methods in Applied Mechanics Engineering* 1974; **3**:269–289.
27. Mompean G, Gavrilakis S, Machiels L, Deville MO. On predicting the turbulence-induced secondary flows using nonlinear k–ε models. *Physics of Fluids* 1996; **8**(7):1856–1868.
28. Rokni M. Personal communication, 1999.
29. Suga K, Nagaoka M, Horinouchi N, Abe K, Kondo Y. Application of a three equation cubic eddy viscosity model to 3-D turbulent flows by the unstructured grid method. *Proceedings of the 3rd International Symposium on Turbulence, Heat and Mass Transfer*, Nagano Y, Hanjalic K, Tsuji T (eds), 2000; 373–380.
30. Andre JC, Moor G De, Lacarrere P, Therry G, Vachat R du. The clipping approximation for inhomogeneous turbulence. *Proceedings of the Symposium on Turbulent Shear Flows*, April 18–20, 1977, Durst F *et al.* (eds), vol. 1. University Park, Pennsylvania, 1977, 4.39–4.46.
31. Runchal AK. CONDIF. A modified central-difference scheme for convective flows. *International Journal of Numerical Methods in Engineering* 1987; **24**:1593–1608.
32. Tucker PG. Assessment of geometric multilevel convergence robustness and a wall distance method for flows with multiple internal boundaries. *Applied Mathematical Modelling* 1998; **22**:193–311.
33. FLUENT 5 User's Guide.
34. Tucker PG. Prediction of turbulent oscillatory flows in complex systems. *International Journal for Numerical Methods in Fluids* 2000; **33**:869–895.
35. Laufer J. Investigation of turbulent flow in a two-dimensional channel. *NACA TN* 1053, 1951.

36. Kim JJ. Investigation of separation and reattachment of turbulence shear layer: Flow over a backward facing step. *Ph.D. Thesis*, University of Stanford, 1978.
37. Brackenridge JB. Transverse oscillations of a liquid jet. *Journal of the Acoustical Society of America* 1960; **32**(10):1237–1242.
38. Chung YM, Tucker PG, Luo KH. Large eddy simulation of complex internal flows. *Proceedings of the DLES-4*, *Workshop on Direct and Large-Eddy Simulation-IV*, July 18–21, 2001; 373–380.
39. Apsley DD, Leschziner MA. A new low-Reynolds-number nonlinear two-equation turbulence model for complex flows. *International Journal of Heat and Fluid Flow* 1998; **19**:209–222.
40. Rokni M, Sunden B. A turbulent heat transfer two-equation model for narrow ducts. *Proceedings of NHTC'00 34th National Heat Transfer Conference*, Pittsburgh, Pennsylvania, 20–22 August, 2000.
41. Abe K, Kondoh T, Nagano Y. A new turbulence model for predicting fluid flow and heat transfer in separating and reattaching flows-II. Thermal field calculation. *International Journal of Heat and Mass Transfer* 1995; **38**(8):1467–1481.
42. Davidson L. Hybrid LES-RANS: a combination of a one-equation SGS model and a k–ω model for predicting recirculating flows. Presented at *European Congress on Computational Methods in Applied Sciences and Engineering*, *ECCOMAS Computational Fluid Dynamics Conference*, Swansea, Wales, UK, 4–7 Sept., 2001.
43. Batten P, Goldberg U, Chakravarthy S. LNS—an approach towards embedded LES. *AIAA Paper*, *AIAA*-2002-0427, 2002.

